

# Solidification of Double-Diffusive Flows Using Thermo-Magneto-Hydrodynamics and Optimization

MARCELO J. COLAÇO<sup>1</sup> AND GEORGE S. DULIKRAVICH<sup>2</sup>

<sup>1</sup>*Department of Mechanical and Materials Engineering, Military Institute of Engineering, Rio de Janeiro, Brazil*

<sup>2</sup>*Department of Mechanical and Materials Engineering, MAIDROC, Florida International University, Miami, Florida, USA*

A multilevel approach, based on our previously developed hybrid optimizer, is presented for solving a problem that consists of a solidifying thermosolutal flow in a square cavity subjected to variable thermal and magnetic boundary conditions. The objective is to reduce the standard deviations of the vorticity within the liquid region as well as reduce the liquid area over the entire domain. Thus, the optimization problem is formulated to simultaneously find thermal and magnetic boundary conditions that must induce such prescribed solute concentration and velocity profiles. The optimizer is based on several deterministic and evolutionary techniques with automatic switching among them, combining the best feature of each algorithm. A radial basis function based response surface scheme is implemented to reduce the overall computing time.

**Keywords** Flow control; Hybrid optimization; Inverse problems; Magnetohydrodynamics; Materials processing; Numerical methods; Smart manufacturing; Solidification; Solute transport.

## 1. INTRODUCTION

In liquids containing a solute, natural convection driven by both temperature and solute concentration gradients in the liquid phase has a considerable influence on the solidification process in multicomponent systems. Temperature gradients may be externally imposed (i.e., by heating/cooling) and are caused internally by the latent heat release or absorption within the mushy zone. The solubility of a component may be variable in solid and liquid phases for multicomponent solutions. Thus, during solidification, a component may be incorporated or rejected, therefore inducing local compositional gradients at the solid–liquid interface. This convective flow, driven by both thermal and solutal buoyancy forces, is commonly recognized as double-diffusive natural convection in solidification. Diverse double-diffusive convection patterns can be generated in the liquid because of different molecular diffusivities of heat and species for most fluids. Variations arise from the boundaries of the moving of the mushy region, the interactions among the heat and mass transfer, fluid flow, and involvement of two distinct phases which have different thermo physical properties.

Many research groups have contributed to this area by studying experimentally [1–6], analytically [7–9], and numerically [10–15] the solidification process in rectangular, trapezoidal, and V-shaped enclosures. Experimental methods play important roles in investigating the solidification process. Mathematical numerical modeling has been and continues to be a powerful tool in improving the understanding of the solidification process.

While growing single crystals from a melt it is desirable that any impurities that originate from the walls of the crucible do not migrate into the mushy region and consequently deposit in the crystal. On the other hand, it is highly desirable to achieve a distribution of dopants in the crystal that is as uniform as possible [16, 17]. Similarly, microsegregation results in the interdendritic spaces when freezing a solute-enriched liquid. It does not constitute a major quality problem of the cast part, since the effects of microsegregation can be removed during subsequent soaking and hot working. Macrosegregation, on the other hand, causes non-uniformity of composition in the cast section on a larger scale [18]. Another example is in the manufacturing of composites and functionally graded materials when it would be highly desirable to have the ability to manufacture composite parts with specified distributions of concentration of micro-fibers or nanoparticles. We have recently demonstrated that control of the distribution of micro-particles and a solute in a thermo-convective flow could be achieved by applying appropriate distributions of magnetic [19–21] fields acting on the electrically conducting fluid containing the solute [22–25].

In this work, we will demonstrate the combined use of optimized thermal and magnetic boundary conditions. The problem consists of a solidifying thermosolutal flow in a square cavity subjected to variable thermal and magnetic boundary conditions where the objective is to reduce the standard deviations of the vorticity and solute concentration within the liquid region as well as reduce the liquid area over the entire domain, thus, maximizing the solidification effect.

Numerical simulations using mathematical models for the combined electro-magneto-hydrodynamics (EMHD) [22, 23] are impossible because of the unavailability of the large number of physical properties that still need to be evaluated experimentally. Therefore, the combined EMHD model has traditionally been divided into two sub-models [24, 25]: a) magneto-hydrodynamics (MHD) that models incompressible fluid flows under the influence of

---

Received August 1, 2006; Accepted January 12, 2007

Address correspondence to George S. Dulikravich, Department of Mechanical and Materials Engineering, MAIDROC, Florida International University, EC 3474, 10555 West Flagler Street, Miami, FL 33174, USA; Fax: +1 (305) 348-6007; E-mail: dulikrav@fiu.edu

an externally imposed magnetic field, while neglecting any imposed electric fields and electrically charged particles, and b) electro-hydrodynamics (EHD) that models the incompressible fluid flows under the influence of an externally imposed electric field, while neglecting any imposed magnetic fields.

In this work we will utilize an MHD model and simultaneously optimize thermal and magnetic boundary conditions in order to achieve desired distributions of solute concentration and vorticity during solidification.

## 2. GENERAL MODEL

In this paper we employed the same methodology derived by Voller et al. [28] for the phase change model. In their paper, they defined three different models: Model A (mushy fluid model), Model B (columnar dendritic with dispersed microstructure model), and Model C (columnar dendritic with distinct microstructure model). In this paper, our equations were based on Voller et al. Model A [28]. A brief review of the basic equations is shown below.

Let us consider a binary mixture, whose schematic phase diagram is given in Fig. 1. The ordinate is the temperature of the mixture, while the abscissa is the concentration of the solute. The origin point of the abscissa corresponds to a pure solvent. Several models exist to model mushy region. Some of them assume that this region is a porous media with variable porosity, while others consider the solid phase to be fully dispersed within the liquid, both having the same velocity, with viscosity rapidly varying within the mushy region.

The liquid and mushy regions are separated by a curve, called the *liquidus line*, which is simplified in this diagram by a straight line. In the same way, the *solidus line* is the line which delineates the solid and mushy regions. Two temperatures are important in this diagram: the first one is the melting temperature of a pure substance, represented by the  $T_m$  in the diagram; the other important point is the eutectic temperature, corresponding to the eutectic concentration. The liquidus line connects the point of melting temperature and zero concentration to the point of eutectic temperature with eutectic concentration.

The model of a physical problem considered here involves laminar natural convection of an incompressible

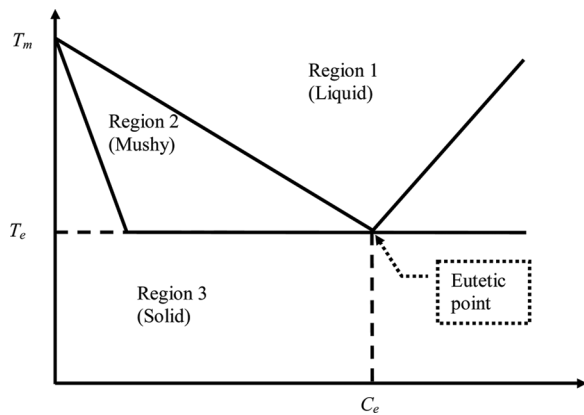


FIGURE 1.—A schematic phase diagram.

Newtonian fluid undergoing a solidification process. The fluid physical properties are assumed constant. The energy source term resulting from viscous dissipation is neglected and buoyancy effects are approximated by the Oberbeck-Boussinesq hypothesis [26, 27]. Radiative heat transfer, Soret and Dufour effects are neglected [26, 27].

The general conservation equations for liquid and solid phases can be written as [28]

$$\frac{\partial}{\partial t}(g_s \rho_s \phi_s) + \nabla \cdot (g_s \rho_s \mathbf{u}_s \phi_s) = \nabla \cdot (g_s \Gamma_s^\phi \nabla \phi_s) + F_s + P \quad (1.a)$$

$$\frac{\partial}{\partial t}(g_l \rho_l \phi_l) + \nabla \cdot (g_l \rho_l \mathbf{u}_l \phi_l) = \nabla \cdot (g_l \Gamma_l^\phi \nabla \phi_l) + F_l - P \quad (1.b)$$

where  $\phi$  is the quantity being conserved,  $g$  is the volume fraction in a representative region,  $\rho$  is the density,  $\Gamma$  is the diffusion coefficient,  $\mathbf{u}$  is the velocity vector,  $F$  is the body force,  $P$  represents the interphase source terms, and the subscripts  $s$  and  $l$  refer to the liquid and solid phases, respectively. Note that the interphase source terms have opposite signs and will cancel out in an additive combination of the phases. The volume fractions  $g_s$  and  $g_l$  are related to the mass fractions,  $f_s$  and  $f_l$ , by [28, 29]

$$\rho f_s = \rho_s g_s \quad \rho f_l = \rho_l g_l \quad (2.a,b)$$

where the local mixture density is defined as

$$\rho = \rho_s g_s + \rho_l g_l \quad (3)$$

The overall conservation equation can be obtained by summing Eqs. (1.a) and (1.b), thus, obtaining

$$\begin{aligned} \frac{\partial}{\partial t}(g_s \rho_s \phi_s + g_l \rho_l \phi_l) + \nabla \cdot (g_s \rho_s \mathbf{u}_s \phi_s + g_l \rho_l \mathbf{u}_l \phi_l) \\ = \nabla \cdot (g_s \Gamma_s^\phi \nabla \phi_s + g_l \Gamma_l^\phi \nabla \phi_l) + F_s + F_l. \end{aligned} \quad (4)$$

For the columnar dendritic zone, a porous media model [28–31] must be employed such that the velocity of the solid phase is imposed as zero. Also, the dissipative interfacial stress is usually modeled in an analogy with Darcy's law, where the permeability is commonly approximated using the Kozeny–Carman equation [28, 29]. This porous media model will not be utilized in this work.

For the mushy zone model [18, 28], which is applicable to amorphous materials (waxes and glasses), and the equiaxed zone of metal casting, the solid is assumed to be fully dispersed within the liquid and that

$$\mathbf{u} = \mathbf{u}_s = \mathbf{u}_l. \quad (5)$$

The velocity within the solid phase is reduced to a negligible level by imposing a large difference of viscosity between the solid and liquid phases, such that

$$\frac{\mu_s}{\mu_l} \geq 10^5. \quad (6)$$

Then, Eq. (4) reduces to

$$\begin{aligned} & \frac{\partial}{\partial t}(g_s \rho_s \phi_s + g_l \rho_l \phi_l) + \nabla \cdot [(g_s \rho_s \phi_s + g_l \rho_l \phi_l) \mathbf{u}] \\ &= \nabla \cdot (g_s \Gamma_s^\phi \nabla \phi_s + g_l \Gamma_l^\phi \nabla \phi_l) + F_s + F_l \end{aligned} \quad (7)$$

If there is an equilibrium among the solid and liquid phases such as  $\phi_l = \phi_s = \phi$  in a representative elementary volume (for example, in the energy equation written for the temperature [29]), then Eq. (7) after using Eq. (3) becomes

$$\frac{\partial}{\partial t}(\rho \phi) + \nabla \cdot (\rho \phi \mathbf{u}) = \nabla \cdot (\Gamma^\phi \nabla \phi) + F \quad (8)$$

where

$$\Gamma^\phi = g_s \Gamma_s^\phi + g_l \Gamma_l^\phi \quad F = F_s + F_l. \quad (9.a,b)$$

### 3. MODEL FOR THE CONCENTRATION EQUATION

In the case of the equation for the concentration, quantities  $\phi_s$  and  $\phi_l$  must obey the binary diagram and Eq. (8) is not valid anymore. For this conservation equation we must use Eq. (7) in its full form.

For the sake of simplicity, let us consider  $\rho_s = \rho_l$  [28, 29]. In the context of solidification, such an assumption will imply no solidification-induced shrinkage [29]. Then, from Eqs. (2) and (7) it follows that

$$\begin{aligned} & \frac{\partial}{\partial t}[\rho(f_s \phi_s + f_l \phi_l)] + \nabla \cdot [\rho(f_s \phi_s + f_l \phi_l) \mathbf{u}] \\ &= \nabla \cdot (f_s \Gamma_s^\phi \nabla \phi_s + f_l \Gamma_l^\phi \nabla \phi_l) + F. \end{aligned} \quad (10)$$

For the mushy region, the concentration of the liquid and solid phases are related through the partition coefficient,  $n$ , defined as [30]

$$C_s = n C_l \quad (11)$$

where  $0 < n < 1$ .

Thus, substituting Eq. (11) in Eq. (10) written in terms of the concentration and knowing that  $f_s = (1 - f_l)$ , it follows, after some manipulations, that

$$\begin{aligned} & \frac{\partial}{\partial t}(\rho C_s) + \nabla \cdot (\rho C_s \mathbf{u}) \\ &= \nabla \cdot (D^+ \nabla C_s) - \frac{\partial}{\partial t} \left[ f_l \left( \frac{1}{n} - 1 \right) \rho C_s \right] \\ & \quad - \nabla \cdot \left[ f_l \left( \frac{1}{n} - 1 \right) \rho C_s \mathbf{u} \right] \end{aligned} \quad (12)$$

where the diffusivity coefficient is

$$D^+ = f_s \rho_s D_s + \frac{f_l \rho_l D_l}{n}. \quad (13)$$

Equation (12) is the same equation proposed by Voller et al. [28] in their Model A. Note, however, that it is only valid for the mushy region and not for the solid and liquid regions. Thus, in order to obtain a model valid for all phases, let us define

$$C = f_s C_s + f_l C_l \quad D = f_s \rho_s D_s + f_l \rho_l D_l. \quad (14.a,b)$$

Equation (14.a) assumes equilibrium (i.e., reversible) solidification. Equilibrium solidification assumes complete mixing in both liquid and solid at every stage of cooling. It also assumes equilibrium at the interface of solid and liquid. Using Eqs. (14), it is possible to rewrite Eq. (10) for the concentration as

$$\begin{aligned} & \frac{\partial}{\partial t}(\rho C) + \nabla \cdot (\rho C \mathbf{u}) = \nabla \cdot (D \nabla C) + \nabla \cdot [f_s \rho_s D_s \nabla (C_s - C)] \\ & \quad + \nabla \cdot [f_l \rho_l D_l \nabla (C_l - C)] \end{aligned} \quad (15)$$

where the last two terms can be written as the source term

$$S_C = \nabla \cdot [f_s \rho_s D_s \nabla (C_s - C)] + \nabla \cdot [f_l \rho_l D_l \nabla (C_l - C)]. \quad (16)$$

The values of the coefficients in this source term depend on the solid and liquid mass fractions,  $f_s$  and  $f_l$ , respectively. In this equation, one must determine the concentration of liquid and solid phases at a given temperature. Considering the liquidus line as a straight line, one can obtain the following equations for the mushy zone by inspecting the binary diagram in Fig. 1.

$$C_l = \frac{T_m - T}{T_m - T_e} C_e \quad C_s = \frac{T_m - T}{T_m - T_e} n C_e. \quad (17, 18)$$

Thus, it is possible to have three different values for the coefficients in the source term given by Eq. (16), depending on which region (liquid, mushy zone, solid) locally exists. These values are summarized in Table 1.

One can check that Eq. (15) reduces to Eq. (12) when  $0 < f_s < 1$ . The solid fraction was modeled by the Lever Rule [30]

$$f_s = \frac{1}{1 - n} \left( \frac{T_l - T}{T_m - T} \right) \quad (19)$$

TABLE 1.—Coefficients for the source terms for the concentration equation.

$f_s$	$f_l$	$C_s$	$C_l$
0	1	0	$C$
1	0	$C$	0
$0 < f_s < 1$	$(1 - f_s)$	Eq. (18)	Eq. (17)

which assumes complete mixing in both liquid and solid phases.

In the Lever Rule, one must determine the temperature of solidification and melting of the mixture at a given concentration. Considering the liquidus line as a straight line, one can obtain the following equation by inspection of the binary diagram in Fig. 1:

$$\begin{aligned} T_l &= T_m - (T_m - T_e) \frac{C}{C_e} \\ T_s &= \text{MAX} \left[ T_e, T_m - (T_m - T_e) \frac{C}{nC_e} \right]. \end{aligned} \quad (20.a,b)$$

Note that, as the solidification begins, the solid phase rejects solute and its concentration in the remaining liquid and especially in the mushy regions increases. Thus, the solid and liquid temperatures at each point of the domain must be determined as the solidification front advances. This indeed induces a buoyancy effect in the Oberbeck–Boussinesq equation. The rejection of the solute by the solid often leads to secondary reactions, such as formation of oxides, sulphides, oxysulphides, and nitrides during solidification, which can significantly alter microsegregation patterns [31]. Such reactions will not be treated in this paper.

#### 4. MODEL FOR THE ENERGY EQUATION

In this work we used the enthalpy method [28] to deal with the phase change problem. In this method, the energy equation appears as a mixed enthalpy-temperature equation. Writing the general conservation Eq. (4) in the enthalpy form where  $\phi = h$ , we have

$$\begin{aligned} \frac{\partial}{\partial t} (g_s \rho_s h_s + g_l \rho_l h_l) + \nabla \cdot (g_s \rho_s \mathbf{u}_s h_s + g_l \rho_l \mathbf{u}_l h_l) \\ = \nabla \cdot (g_s k_s \nabla T_s + g_l k_l \nabla T_l). \end{aligned} \quad (21)$$

Invoking the hypothesis of thermodynamic equilibrium for the temperature implies constant density. In addition, by defining

$$h = g_s h_s + g_l h_l \quad k = g_s k_s + g_l k_l \quad (22.a,b)$$

it is possible to rewrite the energy conservation equation in enthalpy form as

$$\frac{\partial}{\partial t} (\rho h) + \nabla \cdot (\rho \mathbf{u} h) = \nabla \cdot (k \nabla T). \quad (23)$$

Thus, it is necessary to obtain a relationship between the equilibrium temperature and the mixture enthalpy to be used in Eq. (23). For the case of a binary mixture, if  $h < h_{\text{solid}}$ , then

$$T = \frac{h}{C_{Ps}} \quad (24)$$

or, if  $h > h_{\text{liquid}}$

$$T = \frac{h + T_s(C_{Pl} - C_{Ps}) - L}{C_{Pl}} \quad (25)$$

or yet, if  $h_{\text{solid}} < h < h_{\text{liquid}}$

$$T = \frac{h + [T_s(C_{Pl} - C_{Ps}) - L](1 - f_s)}{C_{Pl} + f_s(C_{Ps} - C_{Pl})} \quad (26)$$

where the solid mass fraction,  $f_s$ , is given by Eq. (19), for the Lever Rule Model. Here,  $L$  is the latent heat of liquid–solid phase change.

Note that if  $T < T_{\text{solid}}$ , then  $f_s$  must be set to unity. If  $T > T_{\text{liquid}}$ , then  $f_s$  must be set to zero. The other thermal properties were approximated as linear functions within the mushy region ( $T_{\text{solid}} < T < T_{\text{liquid}}$ ) and kept constant within each phase. Thus, in the mushy region

$$\psi = f \psi_s + (1 - f) \psi_l \quad (27)$$

where  $\psi$  represents, for example, the density, thermal conductivity, viscosity, magnetic permeability, and electric conductivity. For the specific heat at constant pressure within the mushy region, we used the thermodynamic property approximated as [30]

$$C_p = \frac{\partial h}{\partial T} \approx \frac{\sqrt{\left(\frac{\partial h}{\partial x}\right)^2 + \left(\frac{\partial h}{\partial y}\right)^2}}{\sqrt{\left(\frac{\partial T}{\partial x}\right)^2 + \left(\frac{\partial T}{\partial y}\right)^2}}. \quad (28)$$

Note that enthalpy is a function of the temperature which is a function of the solid fraction that is itself a function of the temperature. Thus, if  $h_{\text{solid}} < h < h_{\text{liquid}}$ , we must solve a nonlinear system for  $T$ . From Eqs. (18), (19), and (26) it follows that

$$T - \frac{h + [T_s(C_{Pl} - C_{Ps}) - L] \left[ 1 - \frac{1}{1-n} \left( \frac{T_l - T}{T_m - T} \right) \right]}{C_{Pl} + \frac{1}{1-n} \left( \frac{T_l - T}{T_m - T} \right) (C_{Ps} - C_{Pl})} = 0 \quad (29)$$

for the Lever Rule Model. This equation can be solved for  $T$  by the secant method. It should be pointed out that in this work we have not considered any sink for the momentum due to viscous dissipation in the mushy region. We have also not utilized dynamic computational grid clustering with respect to the solid/melt interface in order to resolve the details of the mushy region.

Once  $T$  is obtained, and knowing the value of  $C$ , the values of the liquid and solid concentrations can be obtained by inspecting the binary diagram given in Fig. 1. After, calculating  $T$  and  $f_s$ , if the local instantaneous mass fraction of solid is equal to zero, then the local instantaneous concentration of the liquid,  $C_l$ , is set to one and the concentration of the solid,  $C_s$ , is set to zero. Otherwise, if the local instantaneous solid fraction is equal to one, then the concentration of the liquid,  $C_l$ , is set to zero and the concentration of the solid,  $C_s$ , is set to one.

## 5. GENERAL SYSTEM OF EQUATIONS

The laminar magneto-hydrodynamic (MHD) natural convection of an incompressible Newtonian fluid with all physical properties assumed constant has a well-known mathematical model involving a combination of Navier–Stokes equations and Maxwell equations [22]. The energy source term resulting from viscous dissipation, radiative heat transfer, and Soret and Dufour effects are neglected. Buoyancy effects are approximated by the Oberbeck–Boussinesq hypothesis [26, 27]. Then, the MHD model in this case can be written, for two-dimensional Cartesian coordinate system, as

$$\frac{\partial Q}{\partial t} + \frac{\partial E}{\partial x} + \frac{\partial F}{\partial y} = S \quad (30)$$

$$Q = \lambda \phi \quad (31.a)$$

$$E = \lambda u \phi^* - \Gamma \frac{\partial \phi^{***}}{\partial x} \quad (31.b)$$

$$F = \lambda v \phi^{**} - \Gamma \frac{\partial \phi^{***}}{\partial y}. \quad (31.c)$$

The values of  $S$ ,  $\lambda$ ,  $\phi$ ,  $\phi^*$ ,  $\phi^{**}$ ,  $\phi^{***}$ , and  $\Gamma$  are given in Table 2 for the equations of conservation of mass, species,  $x$ -momentum,  $y$ -momentum, energy, magnetic flux in the  $x$ -direction, and magnetic flux in the  $y$ -direction.

Note that we used the Oberbeck–Boussinesq approximation [26, 27] for the variation of the density with temperature and concentration in the  $y$ -momentum conservation equation only. Also note that in the energy conservation equation, the term  $C_p T$  was replaced by the enthalpy,  $h$ , per unit mass. This is useful for problems dealing with phase change where we could use the enthalpy method [28].

The above equations were transformed from the physical Cartesian  $(x, y)$  coordinates to the computational coordinate

system  $(\xi, \eta)$  and solved by the finite volume velocity-pressure coupling SIMPLEC method [32]. The WUDS interpolation scheme [33] was used to obtain the values of  $u$ ,  $v$ ,  $h$ ,  $B_x$ , and  $B_y$  as well as their derivatives at the interfaces of each control volume. The resulting linear system was solved by the GMRES method [34] to accelerate the iterative convergence rate.

## 6. VALIDATION OF THE ANALYSIS CODE FOR A TRANSIENT SOLIDIFICATION OF A BINARY MIXTURE

The MHD analysis code was validated against available analytical and experimental benchmark test cases [20, 21, 35–39]. They involved forced convection in regular and irregular channels, natural convection in regular and irregular cavities, forced convection in the presence of magnetic fields (Pouiseuille–Hartmann Flow), phase change in heat conduction and heat convection problems, natural convection in the presence of magnetic fields [16], steady-state cooperating thermosolutal convection in enclosures [4], and transient cooperating thermosolutal convection in enclosures.

Let us now compare the following mathematical model with the results obtained by Voller et al. [28]. They used the SIMPLE method [40] to solve a thermosolutal problem with solidification in a square cavity of size 0.025 m, where all surfaces were insulated, except for the left vertical wall which was suddenly cooled to a temperature below the melting temperature. They used a grid of  $30 \times 30$  cells which, in spite of being very coarse was also used in this work. They did not mention whether they used a clustered grid or not. They also did not mention if they used the co-located or staggered grid scheme. The value of gravity was not given in their paper.

In the Voller et al. paper [28], the initial concentration and temperature inside the cavity was  $T_0 = 600$  K and  $C_0 = 0.1 \text{ kg m}^{-3}$ , respectively. The temperature of the left wall was suddenly imposed and kept at 400 K. All the walls were impermeable to mass. The physical properties representative of an aqueous mixture of ammonium chloride and water

TABLE 2.—Parameters for the Navier–Stokes and Maxwell equations.

Conservation of	$\lambda$	$\phi$	$\phi^*$	$\phi^{**}$	$\phi^{***}$	$\Gamma$	$S$
Mass	$\rho$	1	1	1	1	0	0
Species	$\rho$	$C$	$C$	$C$	$C$	$D$	$\nabla \cdot [f_s \rho_s D_s \nabla (C_s - C)]$ $+ \nabla \cdot [f_l \rho_l D_l \nabla (C_l - C)]$
$x$ -Momentum	$\rho$	$u$	$u$	$u$	$u$	$\mu$	$-\frac{\partial p}{\partial x} - \frac{B_y}{\mu_m} \left[ \frac{\partial B_y}{\partial x} - \frac{\partial B_x}{\partial y} \right]$
$y$ -Momentum	$\rho$	$v$	$v$	$v$	$v$	$\mu$	$-\frac{\partial p}{\partial y} - \rho g [1 - \beta(T - T_0) - \beta_s(C - C_0)]$ $+ \frac{B_y}{\mu_m} \left[ \frac{\partial B_y}{\partial x} - \frac{\partial B_x}{\partial y} \right]$
Energy	$\rho$	$h$	$h$	$h$	$T$	$k$	$\frac{C_p}{\sigma \mu_m^2} \left[ \frac{\partial B_y}{\partial x} - \frac{\partial B_x}{\partial y} \right]^2$
Magnetic $x$ -flux	1	$B_x$	0	$B_x$	$B_x$	$\frac{1}{\mu_m \sigma}$	$\frac{\partial (u B_y)}{\partial y}$
Magnetic $y$ -flux	1	$B_y$	$B_y$	0	$B_y$	$\frac{1}{\mu_m \sigma}$	$\frac{\partial (v B_x)}{\partial x}$

( $\text{NH}_4\text{Cl-H}_2\text{O}$ ) were used.

$$\begin{aligned} C_p &= 3000 \text{ J kg}^{-1} \text{ K}^{-1} & k &= 0.4 \text{ W m}^{-1} \text{ K}^{-1} \\ \mu_l &= 0.001 \text{ kg m}^{-1} \text{ s}^{-1} & \mu_s &= 10000 \text{ kg m}^{-1} \text{ s}^{-1} \\ D &= 4.8 \times 10^{-9} \text{ m}^2 \text{ s}^{-1} & L &= 3 \times 10^5 \text{ J kg}^{-1} \\ \beta &= 4 \times 10^{-5} \text{ K}^{-1} & \beta_s &= 0.025 \\ T_e &= 250 \text{ K} & C_e &= 0.8 & T_m &= 630 \text{ K} & n &= 0.3. \end{aligned}$$

In the original Voller et al. paper [28], the time step for the numerical method was taken as 1.0 second and the final time as 3000 seconds. In the present results, the time step was taken as 0.001 seconds. The stopping criterion at each iteration was taken as the one used by Voller et al. [28]: the mass source within each control volume must be less than  $8 \times 10^{-6}$  and the error in the overall energy and solute balance must drop below  $1 \times 10^{-2}$  and  $1 \times 10^{-4}$  percent, respectively.

In Voller et al. paper [28], transient results were only shown for its Model B, which stands for the columnar dendritic with dispersed microstructure model, while their steady state results were shown for all three models presented in their paper. Figure 2 shows the comparisons

between current results and Voller et al. [28] results where the mass fraction of solid equals to 0.5 at different times, namely,  $t = 100 \text{ s}$ ,  $250 \text{ s}$ , and  $500 \text{ s}$ . For these results, we used Eqs. (12) and (15) for the concentration. Note that we are comparing a mushy zone based model (current results) with a columnar dendritic with dispersed microstructure model (Voller et al. results [28]). However, the results are very similar. The model proposed by Eq. (12), despite being valid only inside the mushy zone, was used in the entire domain. One can see that the locations of the lines of 50 percent of solid phase are in reasonable agreement. However, despite the fact that streamlines are in relative agreement at  $t = 100 \text{ s}$ , they are significantly different at larger times, probably because of the difference between the models. However it is interesting to note that the results are similar for short times, even for different models.

Figure 3 shows the comparison of the macro segregation profiles at  $t = 3000 \text{ s}$  for the original Voller et al. Model A [28] and our current results. One can see that the results are very similar for the case where we used Eq. (12), but are quite different for Eq. (15). The discrepancies between the present results when using Eq. (12) and those presented by Voller et al. [28] can be attributed to different time integration accuracy because of different time step sizes in the present work when compared with the one from Voller et al. [28].

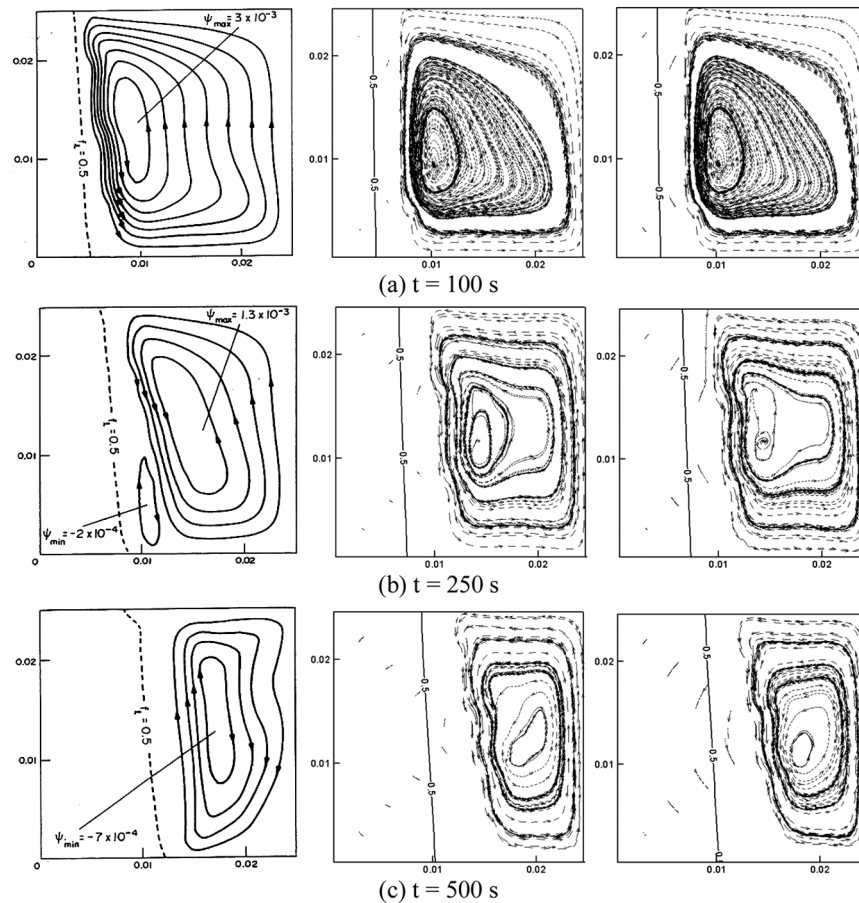


FIGURE 2.—Comparison between Voller et al. [28] (left) and current results (middle and right) for  $f_s = 0.5$ , at different times, utilizing Eq. (12) (middle) and Eq. (15) (right).

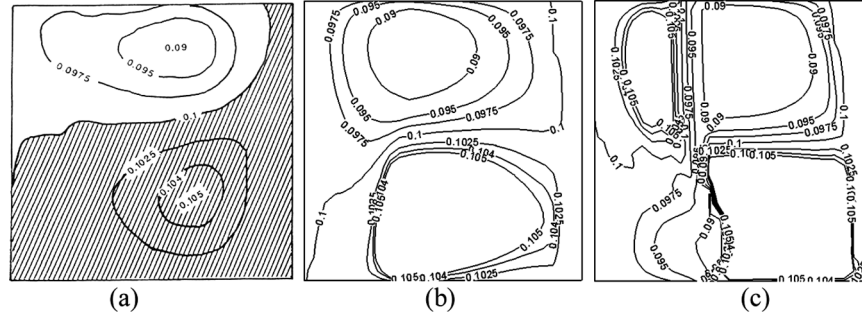


FIGURE 3.—Comparison between Voller et al. [28] (a) and current results for the macro segregation profiles at  $t = 3000$  s, utilizing Eq. (12) (b) and Eq. (15) (c).

## 7. MULTILEVEL HYBRID OPTIMIZER WITH RESPONSE SURFACE

A hybrid optimization is a combination of the deterministic and the evolutionary/stochastic methods, in the sense that it utilizes the advantages of each of these methods. The hybrid optimization method usually employs an evolutionary/stochastic method to locate a region where the global extreme point is located and then automatically switches to a deterministic method to get to the exact point faster. The global procedure is illustrated in Fig. 4. It switches automatically among four different methods of optimization, namely, the Broyden–Fletcher–Goldfarb–Shanno (BFGS) quasi-Newton method [41], the particle swarm method [42], and the differential evolution method [43].

In order to speed-up the optimization task, the optimization procedure starts with a very coarse grid and then proceeds through a sequence of refined grids illustrated in Fig. 5. In this paper we also used an interpolation scheme based on the radial basis function method [44–46]. Thus, after a certain number of objective functions were calculated, all this information was used to obtain a response surface. Such a response surface is then optimized using the same proposed hybrid code so that it fits the calculated values of the objective function as closely as possible.

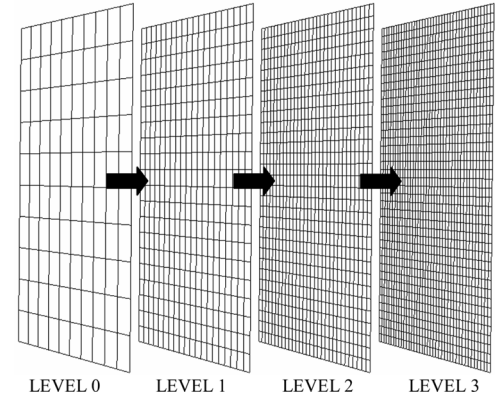


FIGURE 5.—A multilevel optimization sequence of computational grids.

New values of the objective function are then obtained very cheaply by interpolating their values from the response surface.

The most active module in our hybrid optimizer is the particle swarm algorithm which is a nongradient based optimization method created in 1995 as an alternative to the genetic algorithm methods. The original idea came from the observation of birds looking for a nesting place. When the individuality is increased, the search for alternative places for nesting is also increased. However, if the individuality becomes too high, the individual might never find the best place. In other words, when the sociability is increased, the individual learns more from the neighbor's experience. However, if the sociability becomes too high, all the individuals might converge to the first place found (possibly a local minimum).

In the particle swarm method, the iterative procedure is given by

$$\mathbf{x}_i^{k+1} = \mathbf{x}_i^k + \mathbf{v}_i^{k+1} \quad (32.a)$$

$$\mathbf{v}_i^{k+1} = \alpha \mathbf{v}_i^k + \beta \mathbf{r}_{1i}(\mathbf{p}_i - \mathbf{x}_i^k) + \beta \mathbf{r}_{2i}(\mathbf{p}_g - \mathbf{x}_i^k) \quad (32.b)$$

where

$\mathbf{x}_i$  is the  $i$ th individual of the vector of parameters,

$\mathbf{v}_i = 0$ , for  $k = 0$ ,

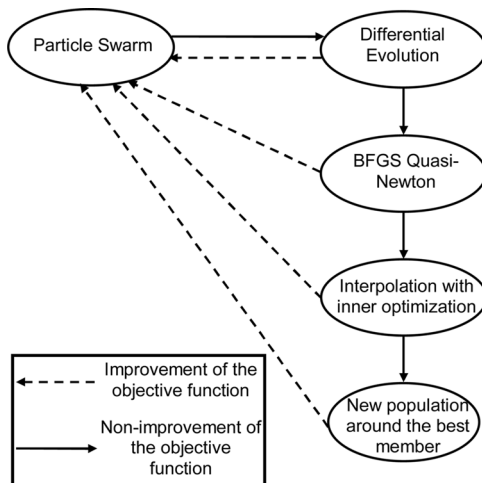


FIGURE 4.—Global procedure for our hybrid optimization method.

$\mathbf{r}_{1i}$  and  $\mathbf{r}_{2i}$  are random numbers with uniform distribution between 0 and 1,

$\mathbf{p}_i$  is the best value found for the vector  $\mathbf{x}_i$ ,

$\mathbf{p}_g$  is the best value found for the entire population,

$0 < \alpha < 1; 1 < \beta < 2$

In Eq. (32.b), the first term on the right-hand side represents the inertia of the particles and, in general, must be decreased as the iterative process proceeds. The second term on the right hand side represents the individuality and the third term the sociability. In this equation, the vector  $\mathbf{p}_i$  represents the best value ever found for the  $i$ th component vector of parameters  $\mathbf{x}_i$  during the iterative process. Thus, the individuality term involves the comparison between the current value of the  $i$ th individual  $\mathbf{x}_i$  and its best value in the past. The vector  $\mathbf{p}_g$  is the best value ever found for the entire population of parameters (not only the  $i$ th individual). Thus the sociability term compares  $\mathbf{x}_i$  with the best value of the entire population in the past.

The differential evolution method [43] is an evolutionary method based on Darwin's theory of evolution of the species. This nongradient based optimization method was also created as an alternative to the genetic algorithm methods. Following Darwin's theory, the strongest members of a population will be more capable of surviving in a certain environmental condition. During the mating process, the chromosomes of two individuals of the population are combined in a process called *crossover*. During this process mutations can occur, which can be advantageous (individual with a better objective function) or disadvantageous (individual with a worse objective function). The mutations are used as a means of escaping from local minima. However, their excessive usage can lead to a nonconvergence of the method. The differential evolution method starts with a randomly generated population matrix  $\mathbf{P}$  in the domain of interest. Thus, successive combinations of chromosomes and mutations are performed, creating new generations until an optimum value is found.

The iterative process is given by

$$\mathbf{x}_i^{k+1} = \delta_1 \mathbf{x}_i^k + \delta_2 [\alpha + F(\beta - \gamma)] \quad (33)$$

where

$\mathbf{x}_i$  is the  $i$ th individual of the vector of parameters,

$\alpha$ ,  $\beta$ , and  $\gamma$  are three members of population matrix  $\mathbf{P}$ ,

randomly chosen,

$F$  is a weight function, which defines the mutation

$(0.5 < F < 1)$ ,

$k$  is a counter for the generations,

$\delta_1$  and  $\delta_2$  delta Dirac functions that define the mutation.

In this minimization process, if  $U(\mathbf{x}^{k+1}) < U(\mathbf{x}^k)$ , then  $\mathbf{x}^{k+1}$  replaces  $\mathbf{x}^k$  in the population matrix  $\mathbf{P}$ . Otherwise,  $\mathbf{x}^k$  is kept in the population matrix.

The binomial crossover is given as

$$\begin{aligned} \delta_1 &= 0, \text{ if } R < CR \\ &1, \text{ if } R > CR, \end{aligned} \quad (34.a,b)$$

where  $CR$  is a user specified factor that defines the crossover  $(0.5 < CR < 1)$  and  $R$  is a random number with uniform distribution between 0 and 1.

In the hybrid optimizer, when a certain percent of the particles find a minimum, the algorithm switches automatically to the differential evolution method and the particles are forced to breed. If there is an improvement in the objective function, the algorithm returns to the particle swarm method, meaning that some other region is more likely to having a global minimum. If there is no improvement of the objective function, this can indicate that this region already contains the global value expected and the algorithm automatically switches to the BFGS method in order to find its location more precisely.

In Fig. 4, if the BFGS cannot find any better solution, the algorithm uses a radial basis function interpolation scheme to obtain a response surface and then optimizes such response surface using the same hybrid algorithm proposed. When the minimum value of this response surface is found, the algorithm checks to see if it is also a solution of the original problem. Then, if there is no improvement of the objective function, the entire population is eliminated and a new population is generated around the best value obtained so far. The algorithm returns to the particle swarm method in order to check if there are no changes in this location and the entire procedure repeats itself. After a specified maximum number of iterations is performed (e.g., five) the process stops. Details of certain parts of this hybrid optimizer as well as other optimizers can be found in a recent tutorial [47].

## 8. INVERSE PROBLEM OF DETERMINING THE UNKNOWN MAGNETIC FIELD BOUNDARY CONDITIONS

In this paper we deal with the inverse determination of the magnetic and thermal boundary conditions that interact with thermal and concentration buoyancies and create such a fluid flow that gives some pre-specified concentration distribution of the solute within a certain region. Figure 6 shows the geometry and the boundary conditions for the

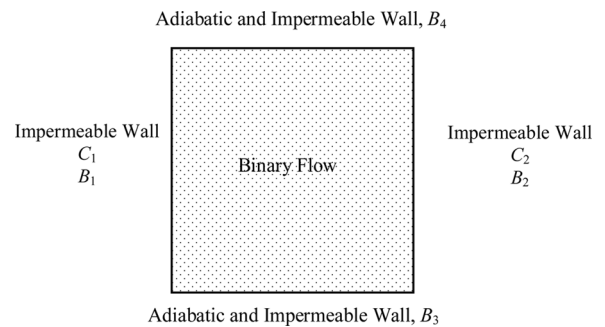


FIGURE 6.—Geometry and boundary conditions for MHD controlled thermosolutal problems.



test cases considered here. The geometry considered is a square cavity, whose height and length are equal to 150 mm. All boundaries were impermeable both to the velocities and to the concentration. The top and bottom walls were kept thermally insulated.

The initial thermal condition was set equal to 1685.04 K throughout the container, while the melting temperature was set to 1685 K. At time zero, left wall temperature was set equal to 1624.96 K. During the optimization process, the temperature of the “hot” right vertical wall was kept constant at 1685.04 K, while the temperature of the “cold” left vertical wall was allowed to vary in the range between 1620 K and 1630 K at each boundary point. Thus, a solidification front starts from the left “cold” wall and a combined buoyancy force due to the thermal and solutal gradients causes the fluid flow.

The objective function was formulated as a multiobjective function. The objective was to solidify the material as fast as possible (thus, “reducing” the liquid area) and also keep the standard deviation of the vorticity ( $\omega$ ) low within the liquid zone (thus, “reducing” the natural convection effects).

Our ultimate objectives are to control local orientations and concentrations of micro particles in the final solid phase. This could be accomplished only if orientations and concentrations of micro particles do not change appreciably in the mushy region while the solidification front passes over such a region. Vorticity causes micro particles in the melt to spin thus causing rapid change in orientation of the micro particles in the melt. Therefore, one of the objectives was to minimize the vorticity in the melt. The objective function that was minimized was then formulated as

$$F = (\text{liquid area fraction})^2 + \sqrt{\frac{1}{\#\text{liquid cells}} \sum_{i=1}^{\#\text{liquid cells}} \left( \frac{\omega_i - \bar{\omega}_i}{\omega_{\max}} \right)^2} \quad (35)$$

where the liquid area fraction varies from 0 to 1 (0 means no liquid area and 1 no solid area). The vorticity was normalized by its maximum value over the entire domain.

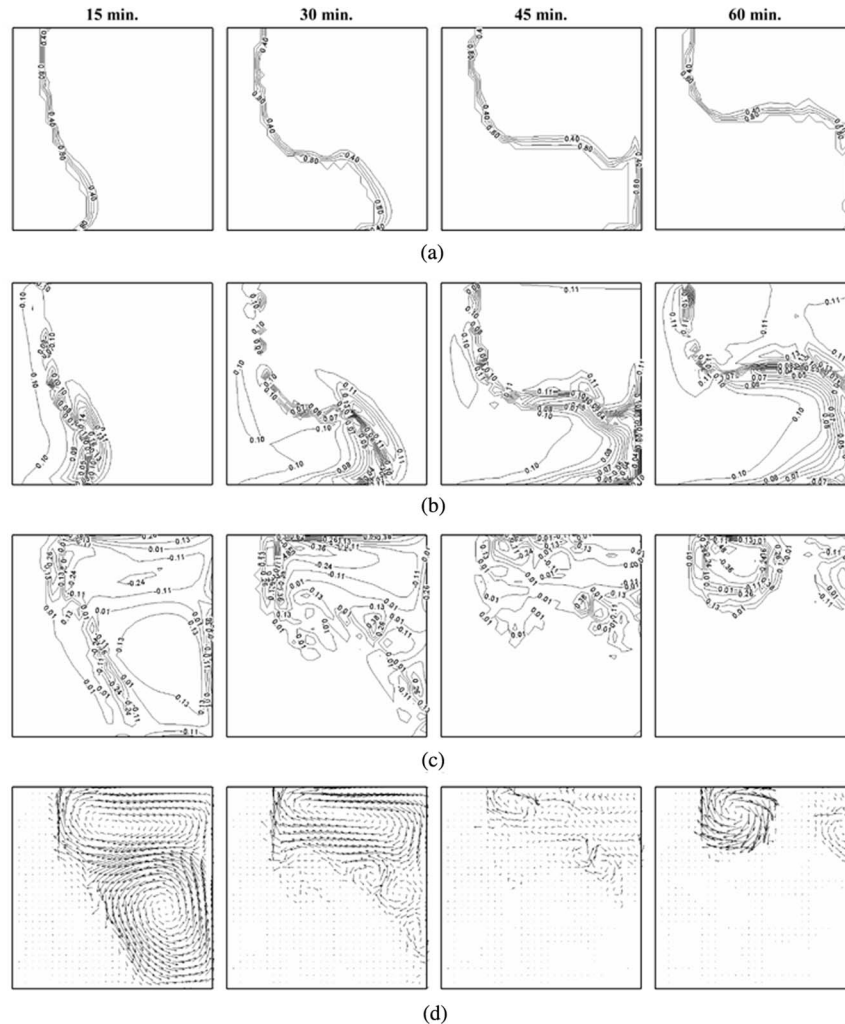


FIGURE 7.—Contours of constant void fractions (a), solute concentration (b), fluid vorticity (c), and velocity vectors (d) with no applied magnetic field ( $\mathbf{B} = 0$ ).

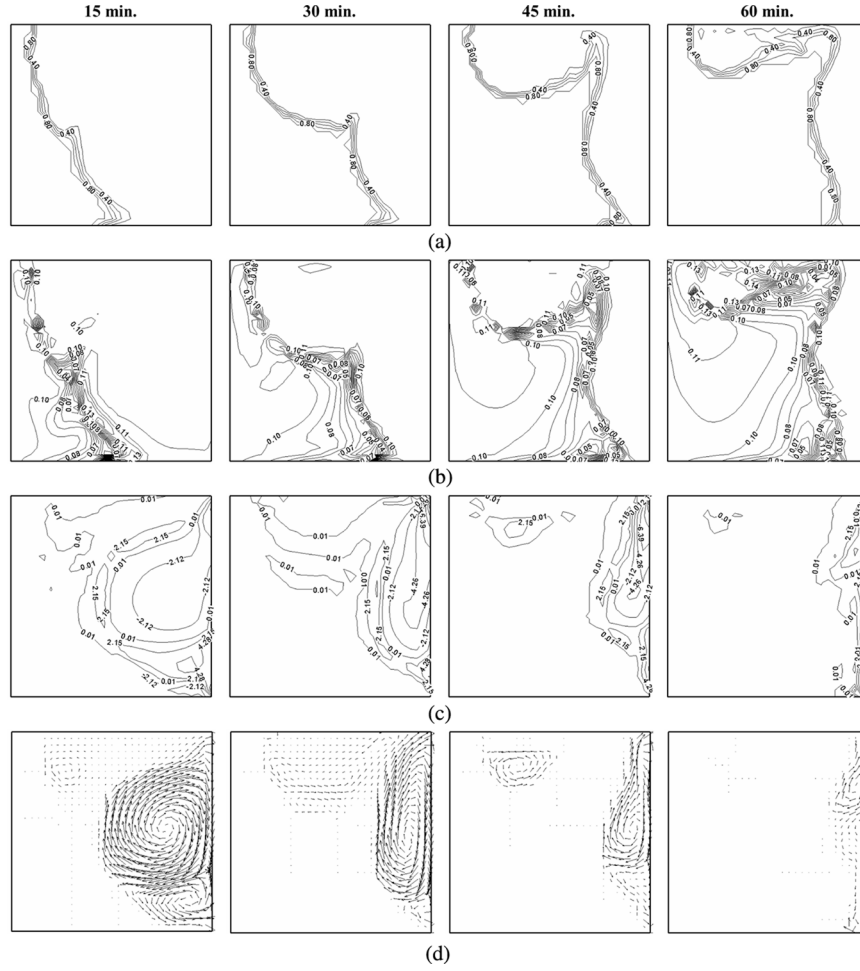


FIGURE 8.—Contours of constant void fractions (a), solute concentration (b), fluid vorticity (c), and velocity vectors (d) resulting from magnetic flux  $B$  optimized at six points per boundary and temperature optimized at six points on the left vertical “cold” wall.

The optimization objectives were to be achieved by allowing simultaneous variation of the normal components of the boundary values of the externally imposed magnetic field on the four walls in addition to allowing the temperature to vary along the “cold” wall. In order to satisfy the magnetic flux conservation equation

$$\nabla \cdot \mathbf{B} = 0 \quad (36)$$

the following periodic conditions were imposed

$$B_1(y) = B_2(y) \quad \text{and} \quad B_3(x) = B_4(x). \quad (37.a,b)$$

The magnetic field and thermal boundary conditions were discretized at six points equally spaced along the  $x = 0.0$  and along  $y = 0.0$  boundaries and interpolated using B-splines for the other points at those boundaries. The magnetic boundary conditions at  $x = 150 \text{ mm}$  and  $y = 150 \text{ mm}$  were then obtained using periodic conditions from Eqs. (37.a) and (37.b). Thus the number of parameters to be optimized were equal to 18 (six for the magnetic boundary conditions at  $x = 0.0$ , six for the magnetic boundary

conditions at  $y = 0.0 \text{ mm}$ , and six for the thermal boundary conditions at  $x = 0.0 \text{ mm}$  – cold wall). The number of individual distributions of thermal and magnetic boundary conditions in the optimization population necessary for the particle swarm method was set equal to 50, which is approximately 2.7 times greater than the number of parameters to be optimized.

The initial condition for the concentration was set equal to  $C_0 = 0.1 \text{ kg m}^{-3}$ . The eutectic temperature and concentration were set to  $1681 \text{ K}$  and  $0.8 \text{ kg m}^{-3}$ , respectively. The equilibrium partition coefficient  $n$  was set to 0.3 and the final time of the simulation was 1 hour.

The physical properties were taken for molten silicon [38] as

$\rho_l = 2550 \text{ kg m}^{-3}$	$\rho_s = 2550 \text{ kg m}^{-3}$
$k_l = 64 \text{ W m}^{-1} \text{ K}^{-1}$	$k_s = 64 \text{ W m}^{-1} \text{ K}^{-1}$
$C_{Pl} = 1059 \text{ J kg}^{-1} \text{ K}^{-1}$	$C_{Ps} = 1059 \text{ J kg}^{-1} \text{ K}^{-1}$
$\mu_l = 0.0032634 \text{ kg m}^{-1} \text{ s}^{-1}$	$\mu_s = 326.34 \text{ kg m}^{-1} \text{ s}^{-1}$
$\sigma_l = 12.3 \times 10^5 \text{ J/m}^2$	$\sigma_s = 4.3 \times 10^4 \text{ J/m}^2$
$\beta = 1.4 \times 10^{-4} \text{ K}^{-1}$	$\beta_s = 0.0875$

$$\begin{aligned}
D_l &= 6.043 \times 10^{-9} \text{ kg m}^{-1} \text{ s}^{-1} & D_s &= 0 \text{ kg m}^{-1} \text{ s}^{-1} \\
g &= 9.81 \text{ m s}^{-2} & \mu_m &= 1.2566 \times 10^{-5} \text{ T m A}^{-1} \\
L &= 1.8 \times 106 \text{ J kg}^{-1}.
\end{aligned}$$

Figure 7 shows the calculated iso-void, iso-concentration, and iso-vorticity profiles and velocity vectors predicted for this test case without any magnetic field applied for four different times:  $t = 15 \text{ min}$ ,  $30 \text{ min}$ ,  $45 \text{ min}$ , and  $60 \text{ min}$ . One can see the large curvature profile for both the void fraction and the concentration lines. A void fraction equals to one represents a pure solid, while a void fraction equals to zero represents a pure liquid. It is worth to note that the solid phase rejects solute to the liquid phase, as the solidification front propagates upwards, as one can see on the bottom of Fig. 7. For this case, the temperature at the left “cold” wall was set to  $1624.96 \text{ K}$ .

Figure 8 shows iso-void, iso-concentration, and iso-vorticity profiles and the velocity vectors resulting from six optimized terms in the B-spline on each boundary for the estimation of the magnetic boundary conditions for four different times. Under the influence of the optimized magnetic field, both the iso-concentration and iso-void fraction profiles are more flat. One can see that the gradients of vorticity are reduced significantly. Using more design variables (B-spline control points) in the optimization could create even better results where the gradients of concentration in the  $y$ -direction would be further reduced. From Fig. 8 is also evident that the velocity field is flatter than the one presented in Fig. 7.

Figure 9 shows the optimized magnetic and thermal boundary conditions for  $x = 0$  and  $y = 0$ . Notice that the strengths of the required magnetic field are very small and could be easily achieved with small permanent magnets. Note also the almost periodic character of the boundary condition for the temperature obtained by the optimizer on the left vertical “cold” wall. It is quite interesting that the algorithm tries to maintain a larger value of the temperature for the upper half of the container, in such a way that this could minimize the natural convection within the liquid area. Note also that the liquid area is reduced when compared with Fig. 8.

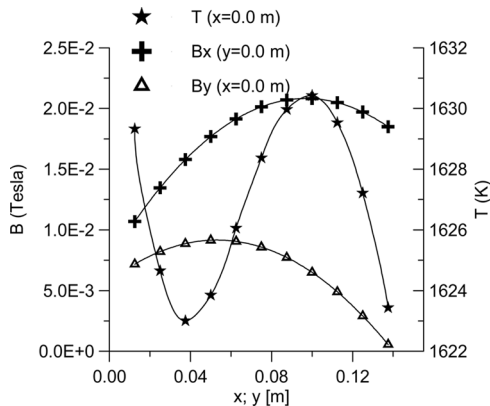


FIGURE 9.—Optimized magnetic and thermal boundary conditions at  $x = 0$  and  $y = 0$  with the estimation of magnetic flux  $\mathbf{B}$  at six points per boundary and estimation of temperature at six points on the left vertical “cold” wall.

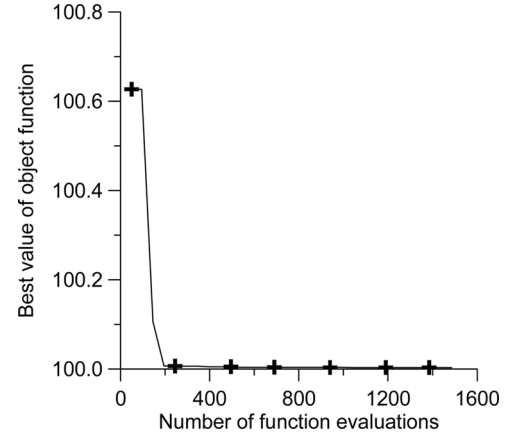


FIGURE 10.—Convergence history of the optimization problem of thermal and magnetic boundary conditions.

Finally, Fig. 10 shows the convergence history, where the number of function evaluations means the number of times that the solver for the Navier and Maxwell equations is called. For these results we used two grids in the multigrid optimizer. The first grid had  $10 \times 10$  cells and the final grid had  $30 \times 30$  cells. The results are presented for the finer grid.

## 9. CONCLUSIONS

In this paper we presented the results of a transient MHD analysis code that is capable of dealing with thermosolutal problems with and without phase change in enclosures. The code was validated against analytical and numerical (benchmark) results showing good agreement and was applied to test cases involving steady state optimization.

1. The ability to minimize the natural convection effects in problems involving phase change was demonstrated by determining an optimized distribution of magnetic and temperature fields applied simultaneously along the boundaries of a solidification container.
2. The practical objective was to solidify the material as fast as possible (thus “reducing” the liquid area) and also keep the standard deviation of the vorticity low within the liquid zone (thus “reducing” the natural convection effects).
3. A response surface hybrid optimization algorithm was used, which reduced the CPU time required for the minimization of the objective function proposed.
4. Transient results were shown where, under the influence of the optimized magnetic and thermal boundary conditions, both the iso-concentration and iso-void fraction profiles became more uniform.
5. It was shown also that the gradients of vorticity were reduced significantly.
6. Due to high computational cost involved in this optimization work, only a coarse computational grid was used in this work. Although the quantitative results were not fully converged, the qualitative behavior was studied and the methodology was demonstrated.

In future works, faster algorithms and a more refined grid should be used. Also, time dependent boundary conditions could be optimized, thus, creating an optimal control algorithm for solidification of binary mixtures.

## ACKNOWLEDGMENTS

This work was partially funded by CNPq (agency for the fostering of science from the Brazilian government). The first author is grateful also for the financial support obtained from Florida International University. Both authors are grateful for the partial financial support provided by the AFOSR grant FA9550-06-1-0170 monitored by Dr. Todd E. Combs and Dr. Fariba Fahroo and by the ARO grant 50486-MS-H monitored by Dr. William M. Mullins.

## REFERENCES

- Cao, W.Z.; Poulikakos, D. Solidification of an alloy in a cavity cooled through its top surface. *Int. J. Heat Mass Transfer* **1990**, *33*, 427–434.
- Chellaiah, S.; Waters, R.A. Solidification of an aqueous salt solution in the presence of thermosolutal convection. *Proceedings of the third ASME-JSME Thermal Engineering Conference*, 2, 1991, pp. 165–174.
- Beckermann, C.; Viskanta, R. An experimental study of melting of binary mixtures with double-diffusive convection in the liquid. *Experimental Thermal and Fluid Science* **1989**, *2* (1), 17–26.
- Skudarnov, P.V.; Lin, C.X.; Wang, M.H.; Pradeep, N. Ebadian, M.A. Evolution of convection pattern during the solidification process of a binary mixture: Effect of initial solutal concentration. *Int. J. Heat and Mass Transfer* **2002**, *45*, 5191–5200.
- Ghenai, C.; Mudunuri, A.; Lin, C.X.; Ebadian, M.A. Double-diffusive convection during solidification of a metal analog system (NH<sub>4</sub>Cl–H<sub>2</sub>O) in a differentially heated cavity. *Experimental Thermal and Fluid Science* **2003**, *28*, 23–35.
- Mergui, S.; Feroual, B.; Gobin, D.; Benard, C. Solidification of a binary mixture in a shear flow. *Int. J. Heat and Mass Transfer* **2004**, *47*, 1423–1432.
- Chakraborty, S.; Dutta, P. An analytical solution for conduction-dominated unidirectional solidification of binary mixtures. *Applied Mathematical Modeling* **2002**, *26*, 545–561.
- Fleming, M.C.; Nereo, G.E. Macrosegregation, Part 1. *Trans. AIME* **1967**, *239*, 50–55.
- Kaviani, M. *Principles of Heat Transfer in Porous Media*; Springer-Verlag: New York, 1991.
- Ni, J.; Beckermann, C. A volume-averaged two-phase model for transport phenomena during solidification. *MetaN. Trans. B* **1991**, *22B*, 349–361.
- Ni, J.; Incropera, F.P. Extension of the continuum model for transport phenomena occurring during metal alloy solidification-I. The conservation equations. *J. Heat and Mass Transfer* **1995**, *38* (7), 1271–1284.
- Ni, J.; Incropera, F.P. Extension of the continuum model for transport phenomena occurring during metal alloy solidification-II. Microscopic considerations. *J. Heat and Mass Transfer* **1995**, *38*, 1285–1296.
- Bennon, W.D.; Incropera, F.P. Numerical simulation of binary solidification in a vertical channel with thermal and solutal mixed convection. *Int. J. Heat Mass Transfer*, **1988**, *31* (10), 2147–2160.
- Sampath, R.; Zabarar, N. Numerical study of convection in the directional solidification of a binary alloy driven by the combined action of buoyancy, surface tension, and electromagnetic forces. *J. Comp. Physics* **2001**, *168* (2), 384–411.
- Heinrich, J.C.; Poirier, D.R. Convection modeling in directional solidification. *Comptes Rendus Mecanique* **2004**, *332* (5–6), 429–445.
- Motakeff, S. Magnetic field elimination of convective interference with segregation during vertical-Bridgman growth of doped semiconductors. *J. of Crystal Growth* **1990**, *104*, 833–850.
- Hirtz, J.M.; Ma, N. Dopant transport during semiconductor crystal growth: Axial versus transverse magnetic field. *J. Crystal Growth* **2000**, *210*, 554–572.
- Ghosh, A. Segregation in cast products. *Sadhana* **2001**, *26*, 5–24.
- Dulikravich, G.S.; Colaco, M.J.; Martin, T.J.; Lee, S.-S. Magnetized fiber orientation and concentration control in solidifying composites. *J. of Composite Materials* **2003**, *37* (15), 1351–1366.
- Colaco, M.J.; Dulikravich, G.S. A multilevel hybrid optimization of magnetohydrodynamic problems in double-diffusive fluid flow. *Proceedings of the Third Meeting of the Study of Matter at Extreme Conditions (SMEC)*; Saxena, S., Ed., Miami Beach, FL, April 17–21, also in *J. Physics and Chemistry of Solids* **2005**, *67*, 1965–1972.
- Colaco, M.J.; Dulikravich, G.S. Obtaining pre-specified concentration profiles in thermosolutal flows by applying magnetic fields having optimized intensity distribution. *Int. Conf. on Computational Methods for Coupled Problems in Science and Engineering, COUPLED PROBLEMS 2005*; Papadarakakis, M., Oñate, E., Schrefler, B., Eds.; Santorini: Greece, 2005.
- Dulikravich, G.S. Electro-magneto-hydrodynamics and solidification. *Advances in Flow and Rheology of Non-Newtonian Fluids, Part B*; Siginer, D.A., De Kee, D., Chhabra, R.P., Eds.; Rheology Series, 8; Elsevier Publishers, 1999; Chapter no. 9, 677–716.
- Ko, H.-J.; Dulikravich, G.S. A fully non-linear model of electro-magneto-hydrodynamics. *Int. J. Non-Linear Mechanics* **2000**, *35* (4), 709–719.
- Dulikravich, G.S.; Lynn, S.R. Unified electro-magneto-fluid dynamics (EMFD): Introductory concepts. *Int. J. Non-Linear Mechanics* **1997**, *32* (5), 913–922.
- Dulikravich, G.S.; Lynn, S.R. Unified electro-magneto-fluid dynamics (EMFD): A survey of mathematical models. *Int. J. Non-Linear Mechanics* **1997**, *32* (5), 923–932.
- Bennacer, R.; Gobin, D. Cooperating thermosolutal convection in enclosures – I. Scale analysis and mass transfer. *Int. J. Heat Mass Transfer* **1996**, *39* (13), 2671–2681.
- Gobin, D.; Bennacer, R. Cooperating thermosolutal convection in enclosures – II. Scale analysis and mass transfer. *Int. J. Heat Mass Transfer* **1996**, *39* (13), 2683–2697.
- Voller, V.R.; Brent, A.D.; Prakash, C. The modeling of heat, mass and solute transport in solidification systems. *Int. J. Heat Mass Transfer* **1989**, *32*, 1719–1731.
- Zabarar, N.; Samanta, D. A stabilized volume-averaging finite element method for flow in porous media and binary alloy solidification processes. *Int. J. for Numerical Methods in Eng.* **2004**, *60*, 1103–1138.
- Rappaz, M. Modelling of microstructure formation in solidification processes. *Int. Materials Review* **1989**, *34*, 93–123.

31. Ghosh, A. *Principles of Secondary Processing and Casting of Liquid Steel*; Oxford and IBH: New Delhi, 1990; Chapters 6, 7, and 9.
32. Van Doormal, J.P.; Raithby, G.D. Enhancements of the SIMPLE method for predicting incompressible fluid flow. *Numerical Heat Transfer* **1984**, 7, 147–163.
33. Raithby, G.D.; Torrance, K.E. Upstream-weighted differencing schemes and their application to elliptic problems involving fluid flow. *Computers and Fluids* **1974**, 2, 191–206.
34. Saad, Y.; Schultz, M. Conjugate gradient-like algorithms for solving non-symmetric linear systems. *Mathematics of Computation* **1985**, 44, 170.
35. Colaço, M.J.; Orlande, H.R.B. Inverse problem of simultaneous estimation of two boundary heat fluxes in parallel plate channels. *J. of the Brazilian Society of Mechanical Sciences* **2001**, 23 (2), 201–215.
36. Colaço, M.J.; Orlande, H.R.B. Inverse forced convection problem of simultaneous estimation of two boundary heat fluxes in irregularly shaped channels. *Numerical Heat Transfer – Part A* **2001**, 39, 737–760.
37. Colaço, M.J.; Orlande, H.R.B. Inverse convection problems in irregular geometries. *Proc. of the 21st Southeastern Conference on Theoretical and Applied Mechanics*, Orlando, Florida, USA, 2002.
38. Dulikravich, G.S.; Colaço, M.J.; Dennis, B.H.; Martin, T.J.; Lee, S. Optimization of intensities and orientations of magnets controlling melt flow during solidification. *J. of Materials and Manufact. Processes* **2004**, 19 (4), 695–718.
39. Colaço, M.J.; Dulikravich, G.S.; Martin, T.J. Control of unsteady solidification via optimized magnetic fields, *Materials and Manufacturing Processes* **2005**, 20 (3), 435–458.
40. Patankar, S.V. *Numerical Heat Transfer and Fluid Flow*; John Benjamins Publishing Co, 1980.
41. Broyden, C.G. Quasi-Newton methods and their applications to function minimization. *Math. Comp.* **1987**, 21, 368–380.
42. Kennedy, J.; Eberhart, R.C. Particle swarm optimization. *Proc. of the 1995 IEEE Int. Conf. on Neural Networks* **1995**, 4, 1942–1948.
43. Storn, R.; Price, K.V. Minimizing the real function of the ICEC'96 contest by differential evolution. *Proc. of IEEE Conf. on Evolutionary Comput.* **1996**, 842–844.
44. Hardy, R.L. Multiquadric equations of topography and other irregular surfaces. *J. of Geophysics Res.* **1971**, 176, 1905–1915.
45. Kansa, E.J. Multiquadrics – A scattered data approximation scheme with applications to computational fluid dynamics – II: Solutions to parabolic, hyperbolic and elliptic partial differential equations. *Comput. Math. Applic.* **1990**, 19, 149–161.
46. Leitão, V.M.A. A meshless method for Kirchhoff plate bending problems. *Int. J. of Numerical Methods in Eng.* **2001**, 52, 1107–1130.
47. Colaço, M.J.; Dulikravich, G.S.; Orlande, H.R.B.; Martin, T.J. Hybrid optimization with automatic switching among optimization algorithms. In: *Evolutionary Algorithms and Intelligent Tools in Engineering Optimization*; W. Annicchiarico; J. Periaux; M. Cerrolaza; G. Winter, Eds.; WIT Press: UK, 2005.